

The study of moving contact line dynamics at obtuse contact angles: An experimental investigation

Charul Gupta,^{1,*} Lakshmana Dora Chandrala,^{1,†} and Harish N Dixit^{1,2,‡}

¹*Department of Mechanical & Aerospace Engineering, Indian Institute of Technology Hyderabad, India*

²*Center for Interdisciplinary Programs, Indian Institute of Technology Hyderabad, India*

(Dated: February 17, 2025)

The flow near a moving contact line is mainly governed by three key parameters: viscosity ratio, dynamic contact angle, and inertia. While the behavior of dynamic contact angles has been extensively investigated in earlier experimental and theoretical studies, very few studies have focused on flow configurations. The present study focuses on obtaining quantitative measurements of flow fields, interface shapes, and interfacial speeds in the low to moderate Reynolds number (Re) regimes using particle image velocimetry and image processing techniques. The study is restricted to dynamic contact angles greater than 90° . In the low Re regime, excellent agreement of streamfunction contours, measured using flow fields, is found with the modified version of the viscous theory of Huh & Scriven [1] that accounts for a curved interface. Theoretical models, such as DRG model, using a single fitting parameter, are shown to predict interface shapes accurately, even at finite Re . The interfacial speed, away from the contact line, compares favorably with the predictions of Huh & Scriven. However, a rapid decrease in speed is observed near the contact line, unlike theoretical predictions. We argue that this rapid reduction in speed is critical to the resolution of the long-standing moving contact line singularity.

Keywords: Stokes flow, dynamic contact angle, contact line dynamics.

I. Introduction

Moving contact line dynamics holds fundamental importance across various fluid flow scenarios. The basic mechanism underlying the dynamics involves the displacement of one fluid phase by another fluid phase (phases A and B) over a solid surface. Numerous applications, ranging from natural phenomena like drops traversing lotus leaves or spreading across solid surfaces to industrial processes such as the deposition of tiny drops onto a piece of paper in inkjet printing, exhibit a similar mechanism. All of these scenarios share a common feature: a moving contact line. The classical work of Huh & Scriven[1] suggested that only two parameters are sufficient to determine the flow field in the vicinity of a moving contact line, the dynamic contact angle (θ_d) and viscosity ratio (μ_A/μ_B). But this theoretical model suffers from a singularity at the contact line. Several theoretical models have been developed to relieve the singularity and also describe the relationship between the dynamic contact angle and the speed of the contact line [2–6]. For example, the viscous study of Cox [5] associated the dynamic contact angle with the capillary number and the logarithm of the ratio of length scales, i.e., $Ca \ln(l_{\text{macro}}/l_s)$, where l_{macro} and l_s are the macroscopic and microscopic length scales, respectively. Several other models have also been proposed over the years and these are summarised in excellent reviews and monographs [7–9].

Few theoretical studies have focused on the flow patterns emerging near the moving contact line. These studies were conducted in the viscous regime by ensuring that both the Reynolds number ($Re = \rho_B U l_{\text{macro}}/\mu_B$) and the capillary number ($Ca = \mu_B U/\sigma$) are much less than unity, i.e., $Re \ll 1$ and $Ca \ll 1$. Here, the subscript B denotes fluid phase B, while ρ represents density, μ denotes viscosity, σ stands for surface tension, and U refers to plate speed. The study by Huh & Scriven (HS71 hereafter) [1] predicted the flow configurations in a local region near the moving contact line by solving the biharmonic equation, assuming standard no-slip boundary condition at the moving solid. One of the key predictions of the HS71 theory was the occurrence of a rolling-type motion in the more viscous phase. However, the theory also suffers a singularity at the moving contact line, where the shear stress diverges. Subsequent theoretical studies were conducted aiming to circumvent the singularity by incorporating new physics at the contact line such as allowing the contact line to slip over the solid or employing a precursor thin film over the solid. For example, the study by Cox [5] employed a constant slip in the slip region near the contact line. Cox divided the local region into three smaller regions using the method of matched asymptotic expansion: a slip, intermediate and outer regions and predicted flow patterns in the intermediate region. The predictions of flow configurations from Cox and other similar theories [10] align closely with the predictions of the HS71 theory. This underscores the significance of HS71 theory and serves as a motivation to test it. The successful testing of the theory will also validate other theoretical studies.

* charul.gupta229@gmail.com

† lchandrala@mae.iith.ac.in

‡ hdixit@mae.iith.ac.in

TABLE I: Operating parameters

Fluid-fluid system	Plate speed U (mm/s)	Reynolds number (Re)	Capillary number (Ca)	Dynamic contact angle θ_d , (deg)	Static advancing angle θ_{sa} , (deg)	Surface property
Air-water	0.5	1.52	6.18×10^{-6}	≈ 94.2	≈ 94	Coated
	1	3.03	1.24×10^{-5}	≈ 97.7	-	Coated
	2	6.07	2.47×10^{-5}	≈ 102.6	-	Coated
	5	15.2	6.18×10^{-5}	≈ 103.6	-	Coated
Air-48 % sugar-water system	0.5	1.25×10^{-1}	8.16×10^{-5}	≈ 95.5	≈ 95	Coated
	1	2.50×10^{-1}	1.63×10^{-4}	≈ 95.7	-	Coated
	2	5×10^{-1}	3.26×10^{-4}	≈ 101.1	-	Coated
Air-60 % sugar-water system	0.10	5.95×10^{-3}	6.96×10^{-5}	≈ 99.1	≈ 99	Coated
	0.15	8.92×10^{-3}	1.04×10^{-4}	≈ 105.2	-	Coated
Air-500cSt silicone oil	2	5.23×10^{-3}	5.58×10^{-2}	≈ 96.8	≈ 12	Uncoated
	3	7.85×10^{-3}	8.38×10^{-2}	≈ 110.4	-	Uncoated

Recent theoretical studies by Kirkinis & Davis [11, 12] employed a variable slip model over a certain distance from the contact line while maintaining the no-slip condition for the remainder of the solid surface. Unlike the study by Kirkinis *et al.*, who investigated the dynamics in a single-phase flow, Febres *et al.* [13] extended the same problem to two-phase flows in their study. They predicted flow configurations in the inner region by solving an eigenvalue problem similar to that in the study by Moffat [14]. The solution reported multiple values of n where each n value corresponds to a different flow configuration, making it challenging to select the appropriate value of n for testing the model. Dynamic interface shapes near the contact line have also been investigated and predicted using theoretical models in the literature. Dussan *et al.* [15] provided a composite solution that integrates the solution from Cox theory [5] with the static interface shape to predict the interface shape across various length scales. In contrast, the study of Chan *et al.* [16, 17] solved a set of differential equations while employing a slip over the solid. They predicted the interface shape at all length scales by applying boundary conditions that ensured an equilibrium contact angle at the contact line and a flat interface in the far field. Both studies require values for tuning parameters to predict the interface shape, making it challenging to predict the interface shape independently. The recent study of Kulkarni *et al.* [18] solved for streamfunctions by employing different slip boundary conditions at the solid surface. A detailed discussion is provided for some of the aforementioned theoretical models in §III.

Earlier theoretical studies have focused on multiple aspects of moving contact line dynamics, such as dynamic contact angles, flow fields, interface shapes, and interfacial speeds. Several experimental studies have also been conducted focusing on similar aspects of the dynamics. The study of Dussan *et al.* [19] inferred the global flow structure inside a liquid drop (honey and glycerol) moving over an inclined plane by tracking the fluid particles at the interface. The classical study of Hoffman [20] uncovered the universal behaviour of dynamic contact angles with capillary number by pushing the different fluid-fluid systems through capillary tubes. Several studies [15, 21, 22], including those by Dussan *et al.*, illustrated the impact of viscous effects on dynamic interface shapes by exhibiting the deviations from static shapes near the contact line. The study by Chen *et al.* [23] reported PIV experiments using 60000 cSt PDMS liquid in the viscous regime and showed a *rolling* type flow configuration near the contact line. Some experimental studies [24, 25] reported dynamic contact angles for drop sliding experiments and compared them with various contact angle models in the viscous regime. However, Puthenveetil *et al.* [26] conducted similar experiments using mercury and water drops, all within the inertial regime. The investigation by Gupta *et al.* [27] indicated a negligible qualitative effect of Re on flow configuration in their brief analysis performed at dynamic contact angles greater than 90° . The recent experimental study of Gupta *et al.* [28] conducted detailed analysis in the viscous regime at low viscosity ratio ($\lambda \ll 1$) and acute dynamic contact angles. Another study by Gupta *et al.* [29] reported two-phase PIV measurements for the first time, primarily focusing on flow configurations at viscosity ratios greater than unity. Both studies concurrently measured flow fields, interface shape, and interfacial speed and rigorously tested the theoretical models. The present study extends the previous two studies by the same authors to the obtuse angle regime, i.e. where the dynamic contact angle is strictly maintained above 90° . The viscosity ratio is kept small and the Reynolds and capillary numbers are varied by varying the speed of the moving plate.

In the present work, we present a thorough investigation of flow dynamics through a systematic variation of the parameters, viscosity ratio and dynamic contact angle. In all experiments, the dynamic contact angles are strictly maintained above 90° , and the viscosity ratios are kept below unity. A plate is immersed in the liquid bath at controlled speeds to obtain low to moderate Re . To the best of our knowledge, no experimental study of this nature has been conducted, except for earlier studies [19, 23], which were performed with very high viscous liquids and at very low speeds to remain within the viscous regime. The current study examines the flow dynamics at low to moderate Reynolds numbers to evaluate the effect of Reynolds numbers on moving contact line dynamics. The experiments are

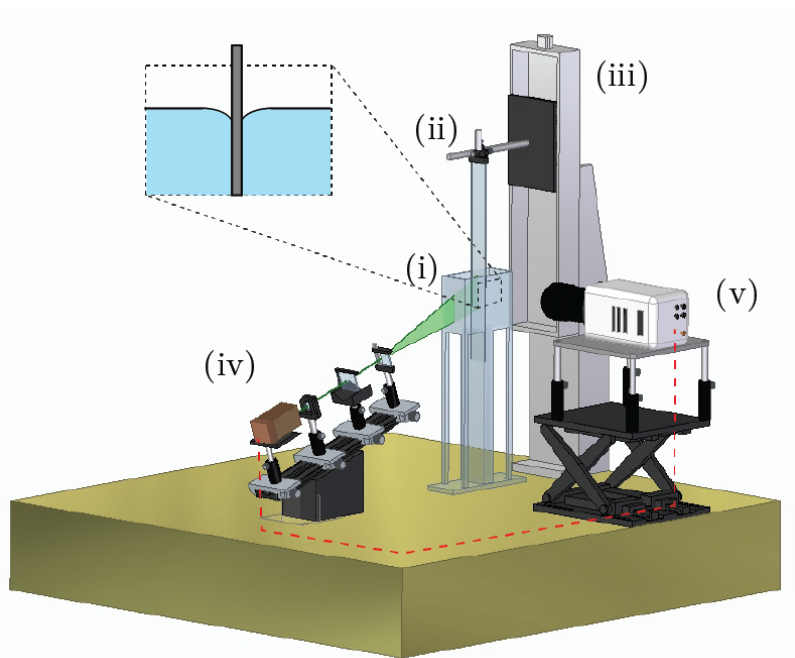


FIG. 1: An illustration of the experimental setup. (i) A transparent acrylic tank filled with liquid (ii) A glass plate traversing into the liquid bath (iii) A linear traversing system (iv) A combination of laser and lens for forming a thin laser sheet (v) High-speed camera. The inset provides a magnified view of the field of interest, showing the fluid phase B forming an obtuse contact angle with the solid surface.

performed with plate immersion configurations to accurately measure the flow fields using the 2D PIV technique, which is nearly impossible in other configurations due to optical issues. The study measures flow fields, interface shapes, and interfacial speeds near the contact line and rigorously compares them against the theoretical predictions. The present study is similar to our earlier study [28], which was performed at acute dynamic contact angles. There are two important reasons for conducting a separate study for obtuse dynamic contact angles: (i) the possibility of observing completely different dynamics, as illustrated by Duez *et al.* [30] in their study, and (ii) water and water-based fluids are widely encountered in natural scenarios, and drops of these liquids typically form obtuse contact angles with solid surfaces while moving. This also serves as a motivation to conduct this study. The present study first time reports the impact of the Reynolds number, Re , on various aspects of moving contact lines by conducting systematic experiments across the parameter space, as provided in Table I. The interfacial speed and the interface shapes measured in our experiments near the contact line can be utilized as boundary conditions for developing numerical and theoretical models.

The paper is structured as follows: §II outlines experimental methodologies and the cleaning procedure. A discussion on the theories related to flow fields and interface shape model is provided in §III. In §IV, comparisons for flow fields, interface shapes, and interfacial speeds against existing theoretical models are presented. Finally, the key findings and important observations are discussed in the §V.

II. Experimental Methodology

The experimental setup is illustrated in figure 1. To facilitate optical measurements, experiments were conducted within a transparent rectangular acrylic tank measuring $100 \times 100 \times 26 \text{ mm}^3$. The tank was filled with liquid (phase B) to a depth of 80 mm. Various liquids, including silicone oil, water, and sugar-water mixtures, were employed to cover a wide range of viscosity ratios, with their properties summarized in Table II. Before the start of each experiment, a glass slide measuring $75 \text{ mm} \times 25 \text{ mm} \times 1 \text{ mm}$ was partially submerged in the liquid pool, establishing a contact line at the intersection of the two phases with the solid substrate. The immersion speed of the solid substrate/plate was controlled by connecting it to a programmable linear traverse. This enabled precise variation of the plate speed from a few microns per second to several centimetres per second, thereby generating a wide range of Reynolds numbers. In order to keep the liquid level constant as the plate submerged, a syringe pump (not shown in figure 1) was used to extract an equivalent volume from the tank.

Water and water-based liquids typically form an acute static contact angle over the glass slide. In experiments

TABLE II: Fluid properties.

	Density kg/m^3	Viscosity $10^{-3} Pa.s$	Surface tension mN.m
Air	1.207	0.0189	-
Water	1000	0.89	72
48% (w/w) Sugar water mixture	1241.76	12.31	75.42
60% (w/w) Sugar water mixture	1330	54.77	78.71
500 cSt Silicone oil	965	516.67	18.5

involving water-based liquids, a hydrophobic coating was applied to the slides to achieve an obtuse contact angle. However, in silicone oil experiments, the obtuse contact angle was achieved by increasing the speed of the slide without requiring any coating on the glass slide. The surface roughness of the slides was determined using a profilometer and found to be in the range of 20 nanometers.

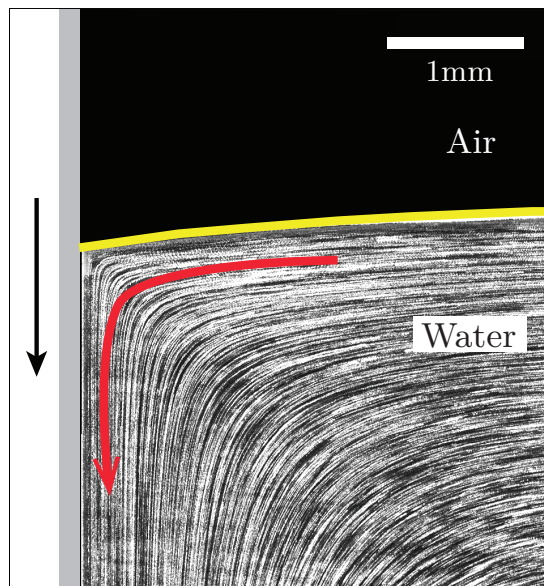


FIG. 2: A streakline image illustrates the flow pattern in the vicinity of a moving contact line at $Re = 3.03$ and $Ca = 1.24 \times 10^{-5}$. As the solid surface, depicted by a grey slab, descends into the liquid, the material points at the interface migrate toward the contact line and subsequently align with the solid surface. The red arrow indicates the flow direction, and the yellow solid curve indicates the air and water interface.

In all the experiments, the same cleaning protocol was followed to eliminate variations. At first, the tank and glass slides were rinsed with distilled water thoroughly and dried using a dryer to avoid any liquid residue. Subsequently, the plate was coated with a hydrophobic coating to obtain a high contact angle over the plate. Following the coating process, the plates were once again rinsed with distilled water and dried with a dryer, which allowed sufficient time for the plate to be in equilibrium with room temperature.

A two-dimensional particle image velocimetry (PIV) technique was utilized to measure the velocity field near the contact line in the mid-plane of the tank (see figure 1). The PIV system comprises a Photron Nova S9 high-speed camera with a resolution of $1024 \text{ pixels} \times 1024 \text{ pixels}$ attached with a macro lens, a green continuous wave diode laser with a maximum power of 2W, and sheet optics. The sheet optics, a combination of biconcave spherical and plano-concave cylindrical lenses, produces a laser sheet of about 0.5 mm thick. In water and water-based experiments, polystyrene particles with an average diameter of $2 \mu\text{m}$ were used as tracers, while for silicone oil experiments, polyamide particles with an average diameter of $5 \mu\text{m}$ were used. The acquisition frame rate of the high-speed camera varied between 50 and 1000 frames per second, depending on the plate speed.

The high-speed camera, coupled with a macro lens attachment, captured a field of view measuring approximately $4.2\text{mm} \times 4.2\text{mm}$, yielding a spatial resolution of $4 \mu\text{m}$ per pixel. Several image processing steps were performed on raw PIV images including average background subtraction and image equalization before a cross-correlation analysis was carried out. Since the flow is steady, the pre-processed PIV images were analyzed using a multigrid and window-deforming ensemble correlation method. A total of 500 images were used to perform ensemble correlation with a final interrogation window size of 16 pixels x 16 pixels.

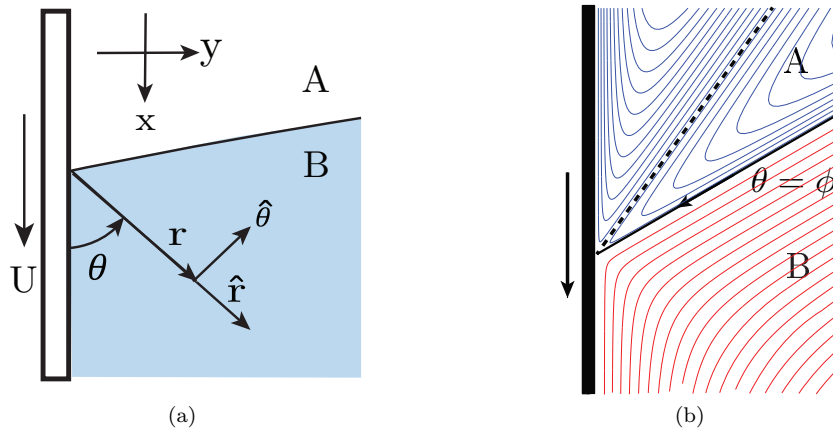


FIG. 3: A schematic diagram of the problem geometry and the flow patterns emerged near the contact line. (a) A solid surface, represented by a black-edged slab, descends into the liquid bath in phase B. The system is characterized by $\hat{r} - \hat{\theta}$ cylindrical coordinate system, where \hat{r} and $\hat{\theta}$ represent the radial and angular coordinates, respectively, with the contact point serving as the origin. An interface between phase A and phase B is depicted by a solid black line at $\theta = \phi$. (b) Considering the advancing motion of the solid, kinematically consistent flow patterns are shown in both phases: split-streamline motion in phase A and rolling motion in phase B.

A sample streaklines image at $Re = 3.03$ and $Ca = 1.24 \times 10^{-5}$ is shown in figure 2. This image was generated by overlaying 500 consecutive particle images and averaging their maximum intensities. The absence of intersecting streaklines indicates a steady flow. The streakline image is further utilized to extract the interface shape and the extracted points were fitted with a two-term exponential function given by

$$y = ae^{bx} + ce^{dx} \quad (1)$$

Here y is the vertical location of the interface (shown with a yellow curve in figure 2) and x is the horizontal distance measured from the vertical plate. The constants a , b , c , and d were determined for each experiment, and in all cases, the two-term exponential fit resulted in an R-square value of close to 0.99. The main purpose of fitting such a function (1) was to extract the local interface angle (slope) which is used in various dynamic contact angle models.

III. Theoretical background

Several theoretical studies have been carried out in the local region near the contact line. Figure 3(a) illustrates this local region at a length scale L , such that $Re_L \ll 1$ and $Ca \ll 1$. The study by HS71 solved the biharmonic equation in the same local region and revealed two key parameters: viscosity ratio and dynamic contact angle. They reported several flow configurations in different regimes of the parameter spaces. A typical flow configuration at an obtuse dynamic contact angle and low viscosity ratio is shown in figure 3(b). Here, fluid particles at the interface move toward the contact line, resulting in a rolling motion in phase B and a split-streamline motion in phase A. Even though HS71 reported stable flow patterns near the contact line, the theory suffers from a stress singularity at the contact line, i.e., $\tau|_{r \rightarrow 0, \theta = 0} \rightarrow \infty$ where τ represents the shear stress. The angle θ is measured from the solid surface in the liquid phase B with the contact line as the origin. Subsequent theoretical studies were conducted using different approaches concentrating on relieving the singularity at the contact line. Several approaches, such as employing a constant slip or a precursor film over the solid near the contact line were utilized. The seminal study of Cox [5] employed a constant slip by dividing the region near the contact line into three sub-regions as shown in figure 4(a), and the solution was obtained using the method of matched asymptotic expansion. The inner region is dominated by slip at the contact line while the outer region depends on the geometry of the problem. The intermediate region, where the no-slip boundary condition applies, matches the inner and outer regions as shown in figure 4(a).

Based on the study by Dussan *et al.* [15], the inner region near the moving contact line governs the flow dynamics in the intermediate and outer regions. However, the reverse is not true. Since the inner region is beyond the range of optical imaging capabilities, understanding the flow configuration in the intermediate region can assist in inferring the configuration in the inner region as well. To ensure the existence of the intermediate region between the inner and outer regions, the following expression, $|Ca \ln(l_s/l_{\text{macro}})| \ll 2$, should hold as explicitly mentioned in the study of Sibley *et al.* [31]. The length scale for the intermediate region (l_i) should satisfy $l_s \ll l_i < l_{\text{macro}}$, where l_s denotes the slip length. In all our experiments, the capillary number, Ca , is kept low ($Ca < 10^{-2}$), and slip length typically falls within the nanometer range. Therefore, the above condition for the presence of a wide intermediate region would

always be satisfied and is accessible in our experiments. The shape of the interface and flow field in the intermediate region can thus be compared against theoretical predictions.

Below we outline the models for interface shape and flow field, and this forms the basis for comparison between experiments and theoretical predictions.

A. Theoretical model for the interface shape

In a static condition, the interface deforms near the contact line due to balance of capillary and gravity forces. However, in a dynamic condition, viscous forces act primarily near the contact line and deforms the interface from its static shape. The deviation of the dynamic interface shape from the static shape is denoted as viscous deformation and is confined to a small region near the moving contact line. Away from the contact line, a balance between surface tension and gravity emerges and the interface shape resembles that of a static meniscus. In the present experimental configuration shown in figure 1, the interface becomes flat and horizontal far away from the moving plate. A model that aims to capture the interface shape in a dynamic setting is required to capture physics both at the moving plate as well as in the far field. Below, we will review two popular models that capture interface shape.

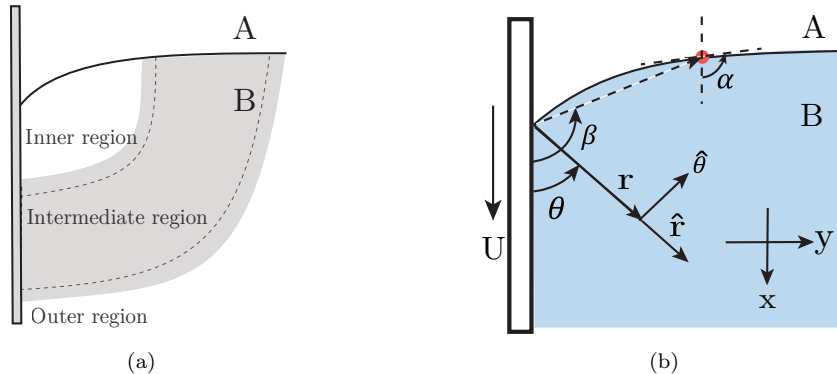


FIG. 4: (a) The cartoon depicts three regions as proposed by the study of Cox [5]. (b) The schematic indicates the problem geometry with the curved interface where the angle β represents the interface angle shown for an arbitrary point on the interface. The angle α represents a local interface slope measured from the vertical direction.

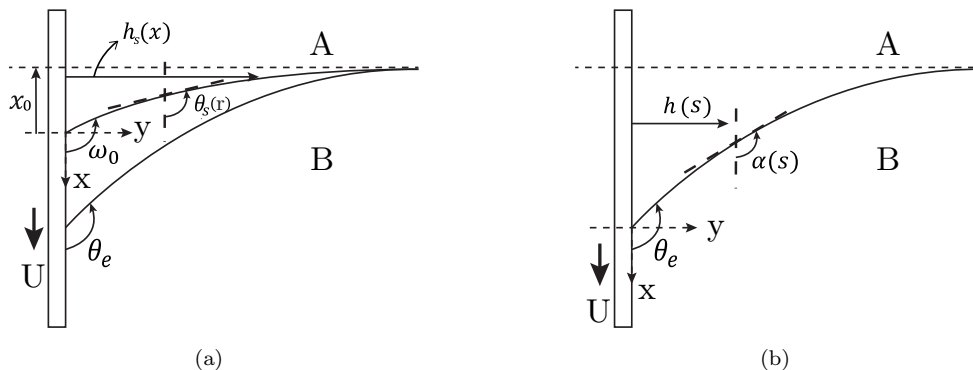


FIG. 5: (a) A schematic represents two interfaces: one with the equilibrium contact angle θ_e at the wall and the other with ω_0 angle at the wall. The latter interface represents the static interface dictated by the outer solution $h_s(x)$ with the contact point as the origin at the wall. The contact angle ω_0 is obtained by matching the inner to the outer region as mentioned in [15]. (b) depicts an interface that forms an equilibrium angle (θ_e) at the contact line while becoming flat in the far field. The interface is dictated by $h(s)$ at any arbitrary arc length s from the origin where contact line is at origin. $\alpha(s)$ denotes a local slope at that arbitrary arc length.

Dussan *et al.*[15] proposed a composite solution for dynamic interface shape by integrating the Cox model, figure 4(a), with the static interface shape. The Cox model accounts for viscous effects, whereas the static shape is influenced by capillary and gravity forces. The incorporation of the static shape enables this model, referred to as DRG model, to predict the interface shape at various length scales. The model predicts the interface shape in terms of the local angle at the interface, i.e. $\alpha(r)$ shown in figure 4(b), at varying radial locations along the interface in the region

spanning from the intermediate to the outer region. The DRG model can be expressed as follows:

$$\alpha(r) = J^{-1} \left[J(\omega_0) + Ca \ln \left(\frac{r}{l_c} \right) \right] + (\theta_s - \omega_0), \quad (2)$$

where l_c denotes the characteristic length, i.e., capillary length and ω_0 represents a tuning parameter. In [15], the value of ω_0 was estimated by minimizing the difference between the interface shape obtained from experiments and the DRG model, i.e. eqn. (2). Physically, one can view ω_0 as the apparent or dynamic contact angle of the system when DRG model is in perfect agreement with experiments.

If viscosity ratio, $\lambda \rightarrow 0$, then the function $J(x)$ can be defined as

$$J(x) = \int_0^x \frac{p - \cos p \sin p}{2 \sin p} dp, \quad (3)$$

The effect of λ is assumed to be negligible for a liquid-gas interface. In eqn. (2), the static interface shape, θ_s , can be expressed by

$$\theta_s = g_0 \left(\frac{r}{l_c}; \omega_0 \right). \quad (4)$$

where θ_s is the local slope from the vertical measured along the static interface (see figure 5(a)). The exact expression for the static shape, given by the function g_0 , formed over flat plate geometry is given in §A. A detailed discussion on the comparison of interface shapes is provided in §IV A.

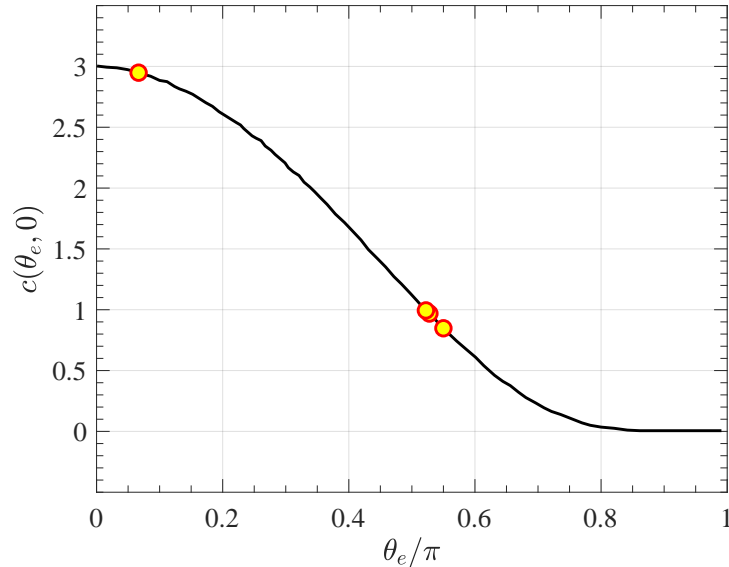


FIG. 6: Variation of c with the static advancing equilibrium angle. A solid black curve is reproduced using Chan *et al.* [17] analysis and filled circles denote our data points where interface shape are compared with GLM as shown in figure 8.

In a recent development, Snoeijer and coworkers [16, 17, 32] developed a generalized lubrication model (GLM) to determine the full interface shape. This model relies on a low capillary number expansion of the Stokes' equations around a constant wedge angle. Unlike classical lubrication theory which is restricted to small interface slopes, the GLM approach can be used for all interface angles. The model reduces to two coupled differential equations for the interface shape, $h(s)$, and the local interface angle, $\alpha(s)$, shown schematically in figure 5(b),

$$\frac{d^2 \alpha}{ds^2} = \frac{3Ca}{h(h + cl_s)} f(\alpha, \lambda) - \frac{1}{l_c^2} \cos(\alpha), \quad (5a)$$

$$\frac{dh}{ds} = \sin(\alpha), \quad (5b)$$

where, s , is the arc length measured along the interface. The singularity at the contact line is regularized by imposing a slip, with slip-length l_s , at the contact line. The constant, c , depends on the equilibrium contact angle. Chan *et al.*

[17] showed that the constant c is approximately equal to 3 for small contact angles and decreases to zero for large contact angles as shown in figure 6. While the general form of the function $f(\alpha, \lambda)$ can be easily used in the solution of eqn. (5), in the present study, $\lambda \ll 1$. We therefore use the $\lambda = 0$ limit in the analysis and the function $f(\alpha, \lambda)$ simplifies to

$$f(\alpha, 0) = -\frac{2 \sin^3(\alpha)}{3(\alpha - \sin(\alpha) \cos(\alpha))}. \quad (6)$$

Using a small capillary number ($Ca \ll 1$), Snoeijer *et al.* [32] integrated eqn. (5) and recovered the expression of the interface shape reported by Dussan *et al.* [15]. While the DRG model requires matching the solutions from two distinct regions to determine the free parameter ω_0 and requires input from the experimental interface shape, the GLM approach eliminates the need for such matching and is thus potentially more attractive. To solve (5), the following boundary conditions on the moving plate and the far-field are employed:

$$\alpha(s=0) = \theta_e; \quad \alpha(s \rightarrow \infty) = \frac{\pi}{2}, \quad h(s=0) = 0. \quad (7)$$

Both DRG model and GLM are compared in detail with experimental interface shapes in §IV A.

B. Theoretical models for flow fields

The HS71 theory provided a solution in a local region near the moving contact line assuming the interface to be flat, with angle ϕ , as shown in figure 3(a). The governing equation, written in the $r - \theta$ coordinate system is given by

$$\nabla^4 \psi = 0, \quad (8)$$

where

$$\psi(r, \theta; \phi) = r(a_1(\phi) \sin \theta + a_2(\phi) \cos \theta + a_3(\phi) \theta \sin \theta + a_4(\phi) \theta \cos \theta). \quad (9)$$

Here, the coefficients a_1, a_2, a_3 and a_4 are functions of the fixed wedge angle ϕ . But in real flows, the interface is often curved. To facilitate a comparison between the HS71 theory and experiments, it is necessary to modify the above solution to accommodate a curved interface. Chen *et al.* [23] proposed modifying the wedge angle, ϕ , in eqn. (9) with the local interface angle, $\beta(r)$ shown schematically in figure 4(b). In a recent study [28], it was shown that this small change in the theoretical expression for streamfunction accounts for curvature effects that are absent in HS71 theory. The modified expression for streamfunction with a curved interface now becomes

$$\psi(r, \theta; \beta) = r(a_1(\beta) \sin \theta + a_2(\beta) \cos \theta + a_3(\beta) \theta \sin \theta + a_4(\beta) \theta \cos \theta). \quad (10)$$

The expression for the coefficients $a_1(\beta) - a_4(\beta)$, is given in §B. If the gas above the interface is assumed to be passive, i.e. viscosity ratio $\lambda \rightarrow 0$, then eqn. (10) greatly simplifies to the form

$$\psi(r, \theta; \beta(r)) = rK(\theta, \beta) = rU \left(\frac{\theta \sin \beta \cos(\theta - \beta) - \beta \sin \theta}{\sin \beta \cos \beta - \beta} \right). \quad (11)$$

The expression for streamfunction for a fixed wedge can simply be obtained by replacing $\beta(r)$ with the fixed wedge angle ϕ as given in eqn. (B1) of §B. The above expression for a curved interface was referred to as ‘modulated wedge solution’ (MWS) by Chen *et al.* [23]. It has to be noted that the interface angle $\beta(r)$ approaches the fixed wedge angle ϕ at the contact line, i.e. $\beta(r)|_{r \rightarrow 0} \rightarrow \phi$. Therefore, the streamfunction expressions for HS71 and MWS theory become identical as one approaches the contact line which is consistent with the view that curvature effects become negligible in the vicinity of the contact line. Unlike in the case of a flat wedge where the interfacial speed coincides with the radial velocity (represented as v_i^{HS} given by eqn. (B2) in §B), the interfacial speed along a curved interface will have both radial (v_r) and angular (v_θ) velocity components (see §C for the expressions) and can be written as

$$v_i^{MWS} = v_r(r, \beta) \cos(\beta - \alpha) - v_\theta(r, \beta) \sin(\beta - \alpha), \quad (12)$$

where $\alpha(r)$ represents the local slope of the interface from vertical (see figure 4(b)) at a radial location r , related to $\beta(r)$ by the following expression:

$$\alpha(r) = \beta(r) + \tan^{-1} \left(r \frac{d\beta}{dr} \right). \quad (13)$$

Using simple geometrical arguments, the expression for interfacial speed can be simplified to

$$v_i^{MWS} = \frac{U}{\cos(\beta - \alpha)} \left(\frac{\sin \beta - \beta \cos \beta}{\sin \beta \cos \beta - \beta} \right). \quad (14)$$

Since the local interface angle $\beta(r)$ varies along the interface, the interfacial speed for a curved interface is not constant unlike the constant value found for a flat interface. Further, at the contact line, $\alpha \equiv \beta$. Thus the interfacial speed for a curved interface (v_i^{MWS}) becomes equal to that of a flat interface (v_i^{HS}) as $r \rightarrow 0$.

Both streamfunctions and interfacial speeds are compared in detail with experimental data in §IV B and §IV C, respectively.

IV. Results

The results are divided into three subsections. In §IV A, we compare the experimental interface shapes against the theoretical model (discussed in §III A). In the subsequent section, in §IV B, we estimate the streamfunctions through the experimental flow fields and compare them by overlaying them with the streamfunctions obtained from the theory. Lastly, in §IV C, tangential speeds along the interface are determined from the flow field data and compared against the theoretical predictions.

A. Interface shape comparison

After the flow has attained a steady state, the interface shape and flow fields are extracted from the PIV data and compared against theoretical predictions. As discussed in section III A, the DRG model is obtained by matching the 'outer' static shape with the inner 'Cox' solution while the GLM only requires the values of the slip length and the contact angle as inputs.

In figure 7, the interface shape from the experiments are compared against the predictions of DRG model for four different values of Ca . At high Ca , shown in figure 7(a), since viscous effects are felt farther away from the moving wall, the Cox model shows substantial 'viscous bending' near the contact line. The large viscous effects also cause the experimental interface shape to deviate from the static shape, and this is often referred to as 'viscous deformation'. The composite DRG solution provides a satisfactory agreement with experimental results except very close to the contact line. The performance of the DRG model improves when the value of Ca is reduced, as is done progressively in figures 7(b), 7(c), and 7(d). At very low Ca , viscous effects are largely confined to very small regions near the contact line, thus the interface shape is largely governed by the static shape as is clearly evident in figure 7. In the low Ca limit, the static shape and the interface shape predicted by the DRG model closely follow the experimental interface shape with an error of $\pm 1^\circ$. Therefore, the algebraic parameter ω_0 in the DRG model will be identical to the dynamic contact angle θ_d . When the experimental and DRG interface shapes are not in perfect agreement, then ω_0 differs from θ_d .

The second approach, the GLM, employs a more direct approach to predict the complete interface shape, as expressed in equations (5). This model requires the slip length l_s as an input parameter, in addition to the constant c that depends on the equilibrium contact angle as shown in figure 6. Since the slip length is unknown, it can be determined by minimizing the deviation between the model's predicted shape and the experimental interface shape. It is important to note that the equilibrium angle, θ_e need not be equal to Young's angle, and in the present case, θ_e is considered equivalent to the static advancing contact angle (θ_{sa}) obtained from direct measurements given in table I. The comparison of interface shapes from the GLM with experimental results is shown in figure 8 for three different slip lengths: 2 nm, 20 nm, and 200 nm. Despite two orders of magnitude variation in slip lengths, the theoretical prediction did not produce any observable deviation in the interface shape.

Figures 8(a) and 8(b) indicate that GLM predictions deviate from experimental results, particularly at high Ca when the equilibrium contact angle is imposed as a boundary condition. The GLM model exhibits pronounced bending of the interface, attributed to the transition from the dynamic contact angle to the equilibrium contact angle at the wall, a phenomenon commonly referred to as viscous bending. However, our experiments reveal no such evidence of viscous bending, at least not at the length scales predicted by GLM. In contrast, for low Ca cases, such as water and sugar-water mixtures, the discrepancy between the dynamic and equilibrium angles is relatively small, leading to better agreement between GLM predictions and experimental observations, as shown in figures 8(c) and 8(d).

Since no viscous bending is visible in the experiments, it is prudent to apply the dynamic contact angle as the relevant boundary conditions in GLM. This requires changing θ_e to θ_d in eqn. 7. This leads to a substantial improvement in the agreement between experiments and GLM predictions as discussed in §D and figure 13.

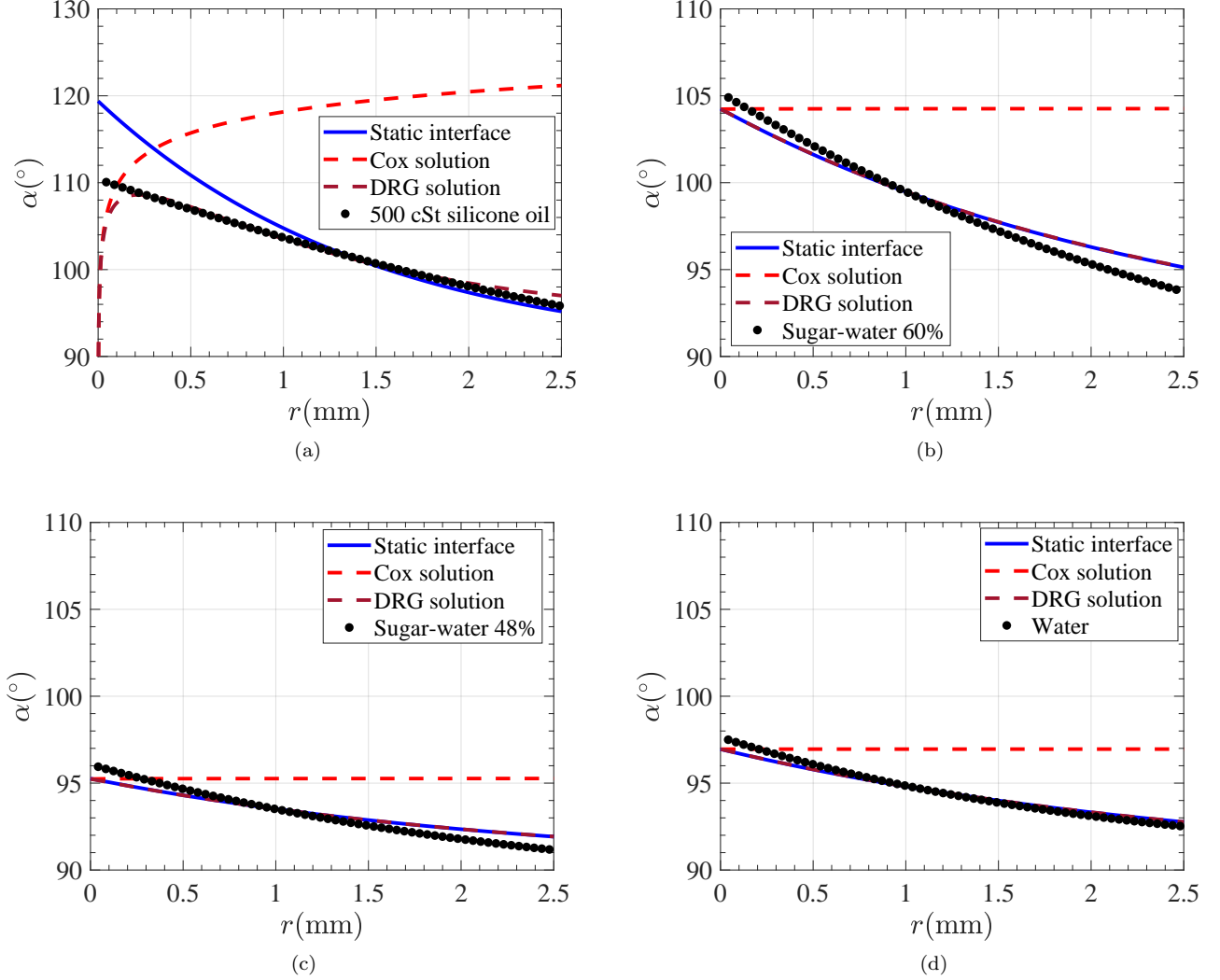


FIG. 7: A comparison of interface shapes among experimental interface shape (dotted black curve), DRG model (maroon dashed curve), Cox model (red dashed curve), and static shape (blue solid curve). (a) air-500 cSt silicone oil at $Ca = 8.37 \times 10^{-2}$, $\omega_0 = 119.4$; (b) air-sugar 60% at $Ca = 1.04 \times 10^{-4}$, $\omega_0 = 104.3$ over a hydrophobic coated surface. (c) air-sugar 48% at $Ca = 8.16 \times 10^{-5}$, $\omega_0 = 95.3$ over a hydrophobic coated solid surface. (d) air-water at $Ca = 1.24 \times 10^{-5}$, $\omega_0 = 96.9$ over a hydrophobic coated solid surface.

B. Comparisons of flow fields

The primary objective of the present study is to examine the flow configurations emerging near the moving contact line. This section aims to compare the flow fields obtained from experiments and the MWS theory. The MWS theory is a modification of the Huh & Scriven's theory adapted to a curved interface. The local interface angle, β as shown in figure 4(b) is obtained from experiments and then incorporated into the MWS theory as discussed in §III. This provides the exact form of the streamfunction in a wedge with a curved interface. The experimental flow fields were obtained through post-processing of particle images acquired from PIV data.

The comparisons are performed by overlaying the streamfunctions obtained from experiments and the MWS theory. The comparison, in terms of streamfunction fields, enables both qualitative and quantitative assessments simultaneously. The qualitative comparison involves matching the superimposed contour shapes, while the quantitative comparison entails the proper alignment of contour shapes with specific contour levels. Such a comparison provides the most rigorous test of theoretical predictions with experimental data. The streamfunction field in experiments were obtained by balancing the mass flux at each consecutive pair of nodes in the flow field data matrix after setting the streamfunction value to zero at the moving wall. The procedure for calculating the streamfunction values is described in more detail in appendix §E. The value of the streamfunction for MWS theory was obtained directly from the

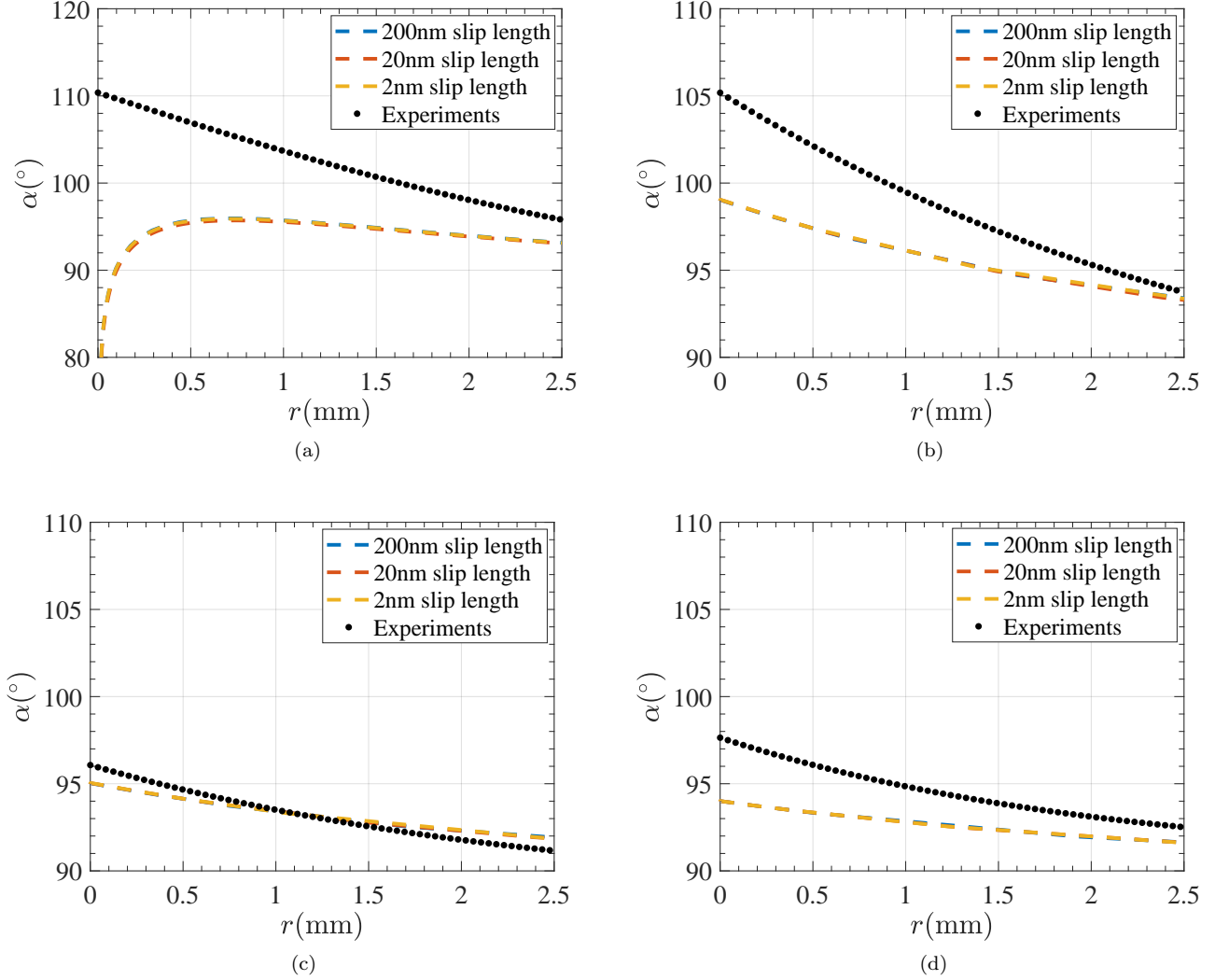


FIG. 8: A comparison of interface shapes between experimental interface shape (dotted black curve) and GLM (dashed curve) with three different slip length 200nm, 20nm and 2nm. (a) air-500 cSt silicone oil at $Ca = 8.37 \times 10^{-2}$, $\theta_e = 12$; $c = 2.95$; (b) air-sugar 60% at $Ca = 1.04 \times 10^{-4}$, $\theta_e = 99$; $c = 0.85$ over a hydrophobic coated solid surface. (c) air-sugar 48% at $Ca = 8.16 \times 10^{-5}$, $\theta_e = 95$; $c = 0.97$ over a hydrophobic coated solid surface. (d) air-water at $Ca = 1.24 \times 10^{-5}$, $\theta_e = 94$; $c = 0.99$ over a hydrophobic coated solid surface.

streamfunction expression mentioned in equn. (11).

A comparison of streamfunction contours between experiments and MWS theory for different fluid-fluid systems is shown in figure 9. These include experiments involving 500cSt silicone oil, 60% (w/w) sugar-water mixture, 48% (w/w)air-sugar-water mixture, and clean water. The accuracy of the theoretical model can be assessed from the agreement of contour shapes and contour levels with experiments. Huh & Scriven’s wedge flow model (presented in the form of MWS) is in fair agreement with experimental observations. In all cases reported in this study, material points at the interface migrate toward the contact line and subsequently align with the moving solid. Similar results were also obtained for all the other liquid-gas combinations given in Table I.

Figures 9(a) and 9(b) illustrate remarkable agreements between MWS theory and experiments for 500cSt silicone oil and 60 % sugar-water mixture, respectively. Here, experimental data is depicted by black solid curves, and MWS theory is depicted by red dashed curves. The comparison is good near the contact line, but deviations become evident as the distance from the contact line increases. Figures 9(c) and 9(d) present streamfunction comparisons for 48% sugar-water mixture and water. Here, the contour levels associated with experimental streamfunctions deviate from the contour levels associated with theoretical streamfunctions. The discrepancies are minimal near the moving solid. However, they become more pronounced as one moves away from the solid and the contact line. Additionally, the experimental streamfunctions appear compressed against the solid surface compared to the streamfunctions derived

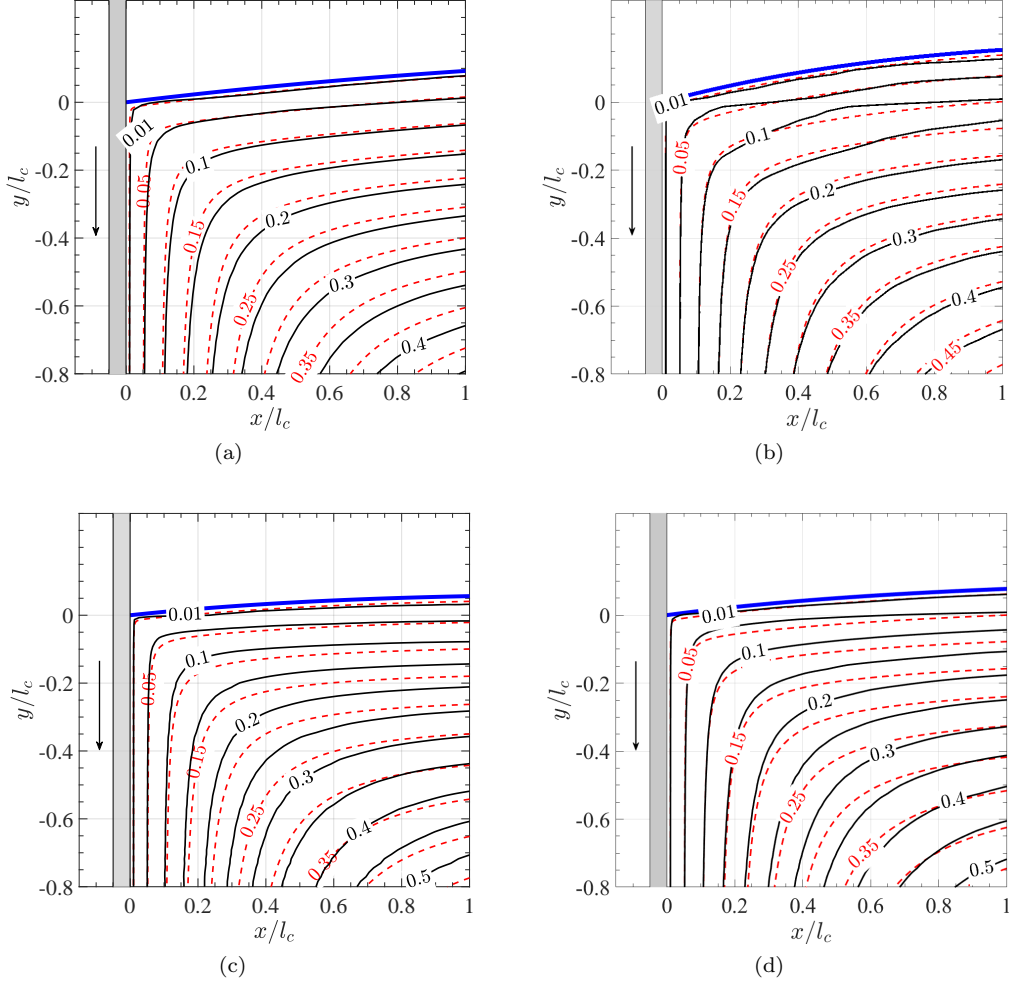


FIG. 9: A comparison between streamfunctions of experiments and MWS theory: (a) 500cSt silicone oil $Re = 5.23 \times 10^{-3}$ and $Ca = 5.58 \times 10^{-2}$. (b) air-sugar-water mixture 60 % (w/w) for coated solid surface at $Re = 8.92 \times 10^{-3}$ and $Ca = 1.04 \times 10^{-4}$. (c) with air-sugar-water mixture 48 % (w/w) for coated solid surface at $Re = 0.125$ and $Ca = 8.16 \times 10^{-5}$. (d) air-water for the coated solid surface at $Re = 3.03$ and $Ca = 1.24 \times 10^{-5}$. Dashed curves are theoretical predictions with levels in red colors. The black solid curves are from experimental data with levels in black color.

from the MWS theory. This discrepancy is observed in 48% sugar-water mixture and water systems, both of which are low-viscosity fluids. These deviations can be attributed to the influence of inertial forces.

The contour plot of $|\psi - \psi_{MWS}|$ provides a quantitative measure of the disparity between the streamfunctions obtained from theory and experiments, as depicted in Figure 10. In both 500 cSt silicone oil and water cases, the difference in the streamfunction values is small near the contact line. This is expected since MWS theory, which in turn is built on HS71 theory, is a local theory. As one moves away from the contact line, inertial effects cannot be ignored. In the case of 500 cSt silicone oil, $Re = 5.23 \times 10^{-3}$ suggests that inertial effects even at a distance of one capillary length are small. But in the case of air-water case shown in figure 10(b), larger differences away in the streamfunction values were observed. This is expected since the Reynolds number based on the capillary length is 3.03 indicating that inertial effects cannot be ignored in this case.

C. Interfacial speed comparison

Interfacial speed refers to the velocity of fluid particles along the interface. The direction of motion of these particles can provide insights into flow patterns within the flow domain through kinematics. Therefore, investigating interfacial speed along the interface is essential. In this study, we estimated interfacial speed by projecting experimental flow field data onto the interface. We compared the experimental interfacial speeds with predictions from both the MWS theory and the HS71 theory. Figure 11 illustrates interfacial speeds for various fluid-fluid systems, including 500 cSt silicone oil, a 60 % (w/w) sugar-water mixture, a 48% (w/w) sugar-water mixture, and water. The interfacial

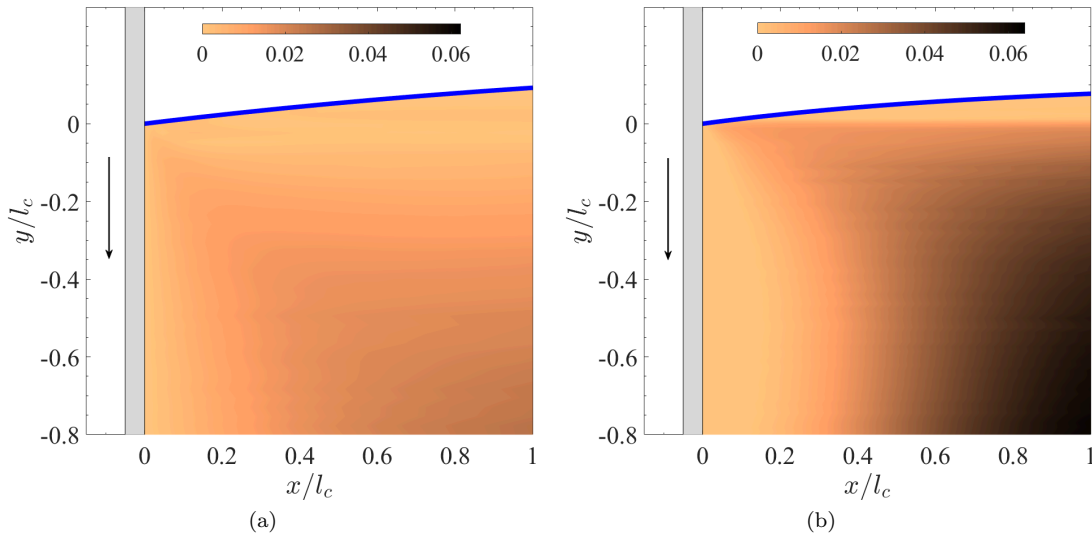


FIG. 10: Difference of non-dimensional streamfunction between theory and experiments, i.e., $|\psi - \psi_{MWS}|$. The streamfunction is non-dimensionalized by Ul_c . (a) streamfunction difference for 500cSt silicone oil at $Re = 5.23 \times 10^{-3}$ and $Ca = 5.58 \times 10^{-2}$ (b) streamfunction difference for air-water at $Re = 3.03$ and $Ca = 1.24 \times 10^{-5}$ with hydrophobic coated surface.

speed, v_t is depicted at several radial positions, r , along the interface, with the contact line taken as the origin. In all experiments, the tangential speed is negative, indicating that the fluid particles are moving toward the contact line. This suggests a global rolling-type motion in the flow domain, consistent with HS71 theory predictions.

The interfacial speeds are compared with predictions from both MWS theory and HS71 theory, as discussed in §III and §B, respectively. HS71 theory predicts a constant interfacial speed, represented by dotted lines, while MWS theory predicts a decreasing interfacial speed along the interface, denoted by solid curves. The MWS theory accounts for curvature effects; however, the deviation in interfacial speed from MWS theory compared to HS71 predictions is not significant. As shown in figure 11(a), the interfacial speeds for the 500 cSt silicone oil and the 60% sugar-water mixture align well with both HS71 and MWS theory predictions. In contrast, the interfacial speed data for the 48% sugar-water mixture and water exhibit slightly higher values compared to predictions from both theories.

These discrepancies in interfacial speeds can be attributed to the wettability of the solid plate, which was coated with a hydrophobic material to maintain an obtuse contact angle. The microscopic contact angle may be higher than the macroscopic angle observed in the experiments, potentially leading to variations in interfacial speed relative to HS71 predictions. For the water system, the interfacial speed shows a decrease in magnitude away from the contact line, which can be attributed to the dominance of inertial forces in the dynamics, particularly given water's low viscosity. Further investigation is required to understand the role of inertia on moving contact lines.

Figure 11(b) provides a magnified view of figure 11(a), focusing on the region within $300 \mu\text{m}$ of the contact line. Notably, within the 100 to $150 \mu\text{m}$ vicinity of the contact line, a sharp decrease in interfacial speed is observed, which does not align with HS71 theory predictions. HS71 theory suggests a constant interfacial speed that maintains its value as one approaches the contact line. As the contact line is approached, the speed should abruptly change direction to align with the plate, resulting in a singularity at the contact line. However, in our experimental observations, a rapid decrease in speed to a low value is noted before alignment with the solid surface. This rapid decrease in interfacial speed near the contact line may provide a potential resolution to the singularity issue.

V. Summary and Discussions

The current study presents simultaneous measurements of flow fields, interface shapes, and interfacial speeds near the moving contact line, comparing these results with earlier theoretical models. These theoretical models were developed within the viscous regime, specifically for conditions where $Re \ll 1$ and $Ca \ll 1$. While the capillary number in the study was always small, varying from 10^{-6} to 10^{-2} , the Reynolds number assumed low to moderate values, varying from 10^{-3} to 10^1 .

The dynamics of the moving contact line depend on parameters such as the viscosity ratio and dynamic contact angles, which were systematically varied through experiments involving different fluid-fluid systems at low to moderate plate speeds. An advancing plate configuration was employed in all experiments to obtain accurate particle image velocimetry (PIV) measurements near the contact line. This configuration is advantageous compared to others, such

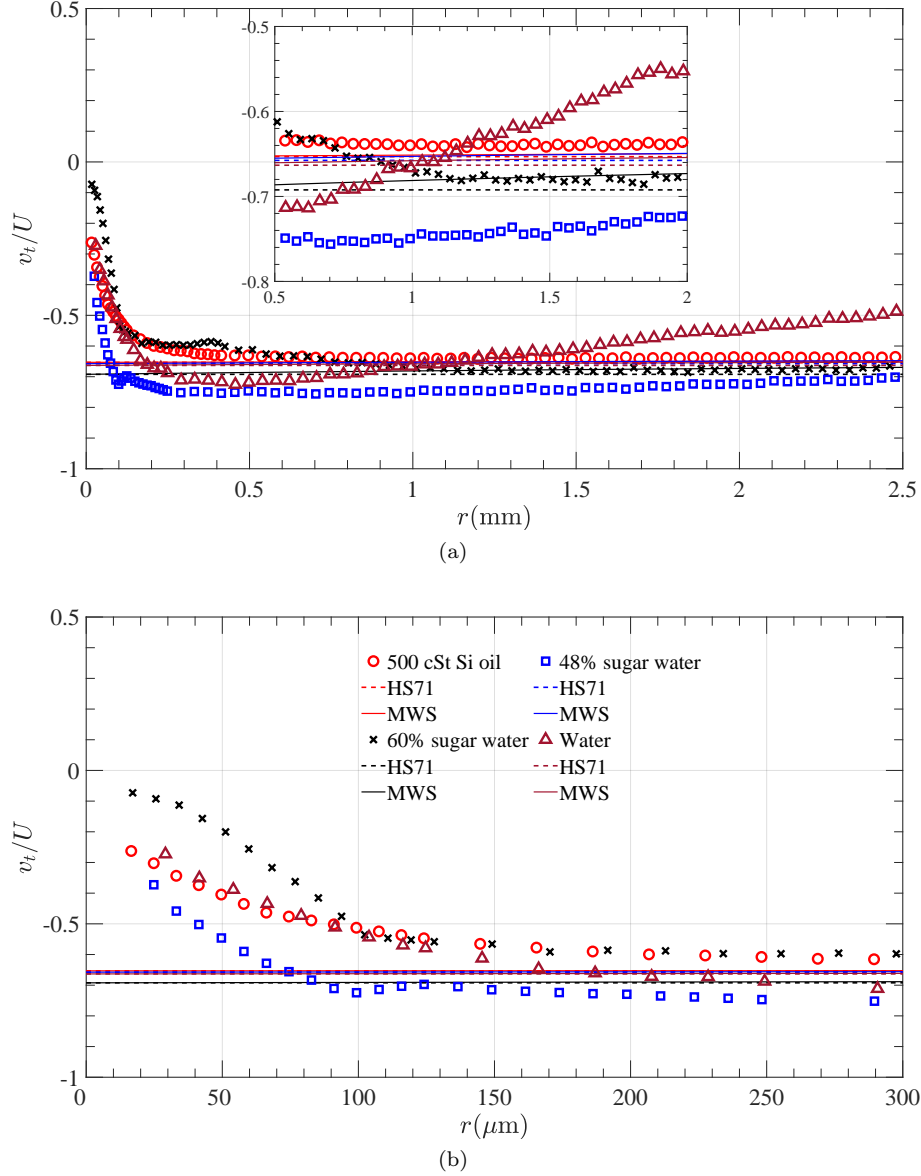


FIG. 11: (a) Non-dimensional tangential speeds (v_t/U) for different fluid-fluid systems, where U is the plate speed. The speeds are measured along the interface, varying with respect to r . The negative values of the speeds indicate the motion of the interface towards the contact line, implying a rolling-type motion in the fluid domain. The inference of flow patterns from the direction of the speed is consistent with the streamfunction contours shown in figure 9. Details of experimental data points are as follows: For 500 cSt silicone oils: \circ : $Re = 5.23 \times 10^{-3}$, $Ca = 5.58 \times 10^{-2}$, $\phi = 96.9^\circ$; For 60% sugar-water mix: \times : $Re = 8.92 \times 10^{-3}$, $Ca = 1.04 \times 10^{-4}$, $\phi = 105^\circ$; For 48% sugar-water mix: \square : $Re = 1.25 \times 10^{-1}$, $Ca = 8.16 \times 10^{-5}$, $\phi = 96.1^\circ$; For water: \triangle : $Re = 3.03$, $Ca = 1.24 \times 10^{-5}$, $\phi = 97.6^\circ$. Interfacial speeds from experiments are denoted with different markers. The predictions from HS71 and MWS theory are shown with dashed lines and solid curves, respectively. The inset shows a close-up view of the interfacial speed away in the far field. (b) A magnified view of interfacial speed near the contact line is shown to emphasize the rapid reduction in the speeds while approaching the contact line.

as droplets moving over an inclined plane or fluids being pushed through a capillary tube, where confined regions hinder the acquisition of precise flow field measurements at larger scales. Additionally, the experiments involving droplets and capillary tubes have to deal with complexities involving image distortion due to curvature of the walls or interface, making PIV measurements challenging. The experiments in this study are performed by immersing a flat plate in a bath of liquid of different viscosities. The primary fluids used in this study were 500 cSt silicone oil, sugar-water mixtures of varying concentrations, and water to obtain a wide range of viscosities.

Theoretical models predict interface shapes across nearly all length scales when $Ca \ll 1$. In this study, experimental interface shapes were compared against the predictions of DRG model and GLM within the low to moderate Ca limit.

At moderate Ca , the DRG model accurately predicts the interface shape away from the contact line; however, deviations occur near the contact line due to the inner physics considered in that region, particularly observed in the case of 500 cSt silicone oil. At very low Ca , the DRG model effectively predicts interface shapes at nearly all length scales, as seen in air-sugar-water and air-water systems. This agreement can be attributed to the viscous effects confined to a few microns near the contact line, which is beyond the resolution of optical technique used in the present study. Consequently, for low Ca , the static interface shape, parameterized in terms of angle ω_0 , is sufficient to predict the experimental shapes across nearly all length scales. On the other hand, GLM approach results in significant deviations from experiments at both low and moderate Ca . As discussed in §III A, GLM employs equilibrium contact angle at the contact line. For highly viscous liquids like 500 cSt silicone oil, the equilibrium contact angle is quite small ($\theta_{sa} \approx 12^\circ$), suggesting that the equilibrium angle may not serve as an appropriate boundary condition in obtuse dynamic contact angle scenarios (see figure 8(a)). GLM does moderately well for low viscous fluids such as water and some combinations of sugar-water mixtures where the equilibrium contact angle is near 90° , but even for these cases, DRG model provides a better fit for the experimental data. It should be noted that GLM relies on viscous effects to determine the interface shape and these effects are primarily confined to regions very close to the contact line. Further GLM does not require information about interface shape from experiments except for the knowledge of slip length. On the contrary, DRG model relies on fitting the static interface shape to the full experimental interface shape. However, since both the interface models show some deviations from the true experimentally determined interface shape, we utilized only the experimental interface shapes for calculating the streamfunction in MWS theory.

Comparisons of flow fields were made in terms of streamfunctions derived from mass conservation across consecutive PIV data points. Streamfunctions obtained from MWS theory and experimental data were overlaid to compare contour shapes, with contour levels facilitating precise quantitative comparisons. Near the contact line, excellent agreement in contour shapes and levels of streamfunctions was observed across all systems. However, deviations emerged as one moved away from the contact line, which is expected since HS71 theory is applicable only in the local region very close to the moving contact line.

The experimental interfacial speeds, extracted from the flow fields by projecting them onto the interface, were compared with predictions from both HS71 theory and MWS theory. For highly viscous fluids such as 500 cSt silicone oil and a 60% sugar-water mixture, the experimental interfacial speeds exhibited reasonable agreement with theoretical predictions, particularly away from the contact line. Close to the contact line, the experimental interfacial speeds decreased rapidly to a very small value, facilitating a smooth alignment of the fluid with the solid. This observation contrasts with the HS71 theory prediction, which anticipates a constant speed at the contact line, necessitating an infinite force to align the fluid with the solid and leading to a singularity. The sharp deceleration of experimental interfacial speed near the contact line offers direct experimental evidence of the long-standing problem of the moving contact line singularity. A similar deceleration trend was observed in low-viscosity fluids, such as in systems using 48% sugar-water mixture and water, although interfacial speeds deviated from HS71 theory away from the contact line. Experimental interfacial speeds for both the 48% air-sugar-water mixture and air-water systems were found to be higher than HS71 theory predictions. This discrepancy may be attributed to surface wettability, as a hydrophobic coating was applied to the plate for the sugar-water mixture and water systems to maintain an obtuse contact angle. Thus, the microscopic angle at the plate may be higher than the macroscopic angle observed in experiments, potentially increasing interfacial speed. For the air-water system, the interfacial speed displayed a decrease in magnitude following an initial increase away from the contact line, attributed to inertial forces dominating the dynamics in this low-viscosity fluid.

In summary, the investigation demonstrates that the viscous theory proposed by HS71 can qualitatively predict flow dynamics effectively, even at moderate Re . The flow fields, interface shapes, and interfacial speeds for highly viscous fluids align well with theoretical predictions; however, deviations are noted for low-viscosity fluids.

Acknowledgments

We wish to acknowledge the support of the Science and Engineering Research Board (SERB), Dept. of Science and Technology, India, for funding this research through grant no. CRG/2021/007096.

DATA AVAILABILITY

The data that support the findings of this study are available from the corresponding author upon reasonable request.

A. The expression for static interface shape

A static interface shape for flat plate geometry can be represented in a parametric form as follows:

$$\theta_s(r) = \frac{\pi}{2} - \tan^{-1} \left(\frac{dh_s}{dx} \right), \quad (\text{A1})$$

In the given expression, θ_s represents a local slope from the vertical direction (see figure 5(a)), with the subscript s indicating a static solution. h_s and x denote the non-dimensional horizontal and vertical location of an arbitrary point on the static interface, respectively.

The full nonlinear Young-Laplace equation can be written expressing the h_s in terms of x and x_0 as

$$h_s(x) = l_c \left[\cosh^{-1} \left(\frac{2l_c}{x_0 - x} \right) - \cosh^{-1} \left(\frac{2l_c}{x_0} \right) \right] - (4l_c^2 - (x_0 - x)^2)^{1/2} + (4l_c^2 - x_0^2)^{1/2}, \quad (\text{A2})$$

where

$$x_0 = \sqrt{2}l_c (1 - \sin \omega_0)^{1/2}. \quad (\text{A3})$$

Here, l_c is the characteristic length (capillary length in the present study), and x represents the vertical location of the interface, which starts from 0 at the contact line to x_0 in the far field. ω_0 denotes an apparent angle measured at $x = 0$ and determined through an iterative error minimization process.

B. The expressions of streamfunction and interfacial speed for fixed wedge geometry

Coefficients of streamfunction equation for fluid phase B are as follows:

$$\begin{aligned} a_1 &= \frac{1}{\sin \beta} (-a_3 \beta \sin \beta - a_4 \beta \cos \beta) \\ a_2 &= 0 \\ a_3 &= \frac{1}{\beta} \left(U + a_4 \left(1 - \beta \frac{\cos \beta}{\sin \beta} \right) \right) \\ a_4 &= \frac{U \sin \beta \cos \beta}{\Delta} \left(\sin^2 \beta - \delta^2 + \lambda (\delta \beta - \sin^2 \beta) - \lambda \pi \tan \beta \right) \end{aligned}$$

where $\Delta = (\sin \beta \cos \beta - \beta)(\delta^2 - \sin^2 \beta) + \lambda(\beta^2 - \sin^2 \beta)(\delta - \sin \beta \cos \beta)$ and $\delta = \beta - \pi$.

Streamfunction expression for a fixed wedge is obtained by solving the biharmonic equation with the standard no-slip boundary condition over the moving wall. The resulting expression for the streamfunction is as follows:

$$\psi(r, \theta; \phi) = rK(\theta, \phi) = rU \left(\frac{\theta \sin \phi \cos(\theta - \phi) - \phi \sin \theta}{\sin \phi \cos \phi - \phi} \right). \quad (\text{B1})$$

In all our experiments, phase A is air, which has very low viscosity. Therefore, the equn. B1 is formulated by considering the air or gas above the liquid as passive, i.e., $\lambda = 0$. The interfacial speed, v_i^{HS} , is determined by setting the angle θ as $\theta = \phi$ and it is given by:

$$v_i^{HS} = v_r(r, \phi) = U \left(\frac{\sin \phi - \phi \cos \phi}{\sin \phi \cos \phi - \phi} \right). \quad (\text{B2})$$

Here, U is the plate speed, and ϕ is the contact angle for the fixed wedge. Note that the expression for interfacial speed is independent of radial position r . Hence, the interfacial speed for the fixed wedge is constant along the interface.

C. The expressions for velocity components v_r and v_θ for curved wedge geometry

The fixed contact angle ϕ in the streamfunction expression (see equn.B1) is replaced with interface angle $\beta(r)$ to incorporate the curvature effects. The velocity components v_r and v_θ can be expressed as:

$$v_r(r, \theta; \beta) = \frac{\partial K}{\partial \theta}, \quad (\text{C1})$$

$$v_\theta(r, \theta; \beta) = -K - r \frac{\partial K}{\partial \beta} \frac{\partial \beta}{\partial r}, \quad (\text{C2})$$

Using the expression for $K(\theta, \beta)$ from equn. 11, we have

$$\frac{v_r(r, \theta; \beta)}{U} = \frac{\sin \beta \cos(\theta - \beta) - \beta \cos \theta - \theta \sin \beta \sin(\theta - \beta)}{\sin \beta \cos \beta - \beta}, \quad (\text{C3})$$

$$\frac{v_\theta(r, \theta; \beta)}{U} = \frac{\beta \sin \theta - \theta \sin \beta \cos(\theta - \beta)}{\sin \beta \cos \beta - \beta} + r \frac{d\beta}{dr} \left(\frac{2 \sin^2 \beta (\beta \sin \theta - \theta \sin \beta \cos(\theta - \beta))}{(\sin \beta \cos \beta - \beta)^2} - \frac{\theta \cos(2\beta - \theta) - \sin \theta}{\sin \beta \cos \beta - \beta} \right). \quad (\text{C4})$$

D. Interface shape from GLM using dynamic contact angle

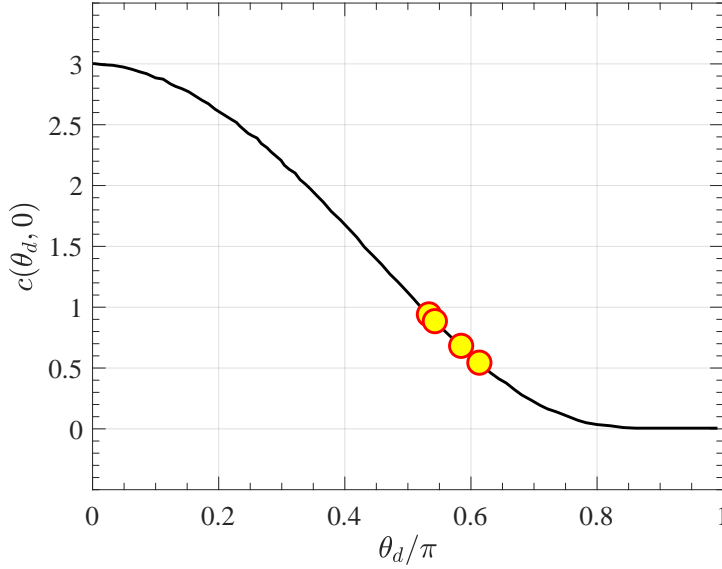


FIG. 12: Same as figure 6 with only difference in contact angle employed at the contact line. Dynamic contact angle (θ_d) is used instead of θ_e . Here, the filled circles denote our data points where interface shape are compared with GLM as shown in figure 13.

In §IV A, the generalized lubrication model was compared with experimental data using the static advancing contact angle. Using the static advancing angle was justified on the grounds that in the vicinity of the contact line where bulk motions cease to exist, the relevant contact angle boundary condition would be the microscopic or static (advancing) contact angle. In the present section, we present the comparison of experimental data with GLM solution, but with the dynamic contact angle. These GLM solutions are obtained by solving equations (5) - (7), but with θ_e replaced with θ_d in equn. 7. The constant c also changes for the different cases and is shown in figure 12 and the comparison of interface shapes is shown in figure 13. The main difference between figure 8 and 13 can be seen in the vicinity of the contact line, i.e. as $r \rightarrow 0$. The large difference between ‘equilibrium’ and dynamic contact angles between figures 8(a) and 13(a) produces significant difference in the values of the constant c , 2.95 and 0.54 respectively. This leads to large variation in the interface shapes from GLM for the two cases. Further, for figure 13(a), the GLM solution over predicts the dynamic contact angle and a sharp ‘boundary’ layer is produced as $r \rightarrow 0$. Less deviation is observed for figures 13(b), 13(c) and 13(d) from its counterpart in figure 8.

E. Streamfunction calculation from PIV data

As is well known, PIV data produces a vector image with velocity field laid on a uniform grid of points. If $u(x, y)$ and $v(x, y)$ represent the horizontal and vertical components of a steady-state velocity field obtained from experiments, it is possible to determine the streamfunction $\psi(x, y)$ from this velocity field by using mass conservation. If \dot{q} is the mass flux between any two points, say, 1 and 2, then it is well known that $\psi_1 - \psi_2 = \dot{q}$. Using this principle, we calculate the mass flux between a pair of grid points sequentially and determine the function $\psi(x, y)$ in the entire flow domain.

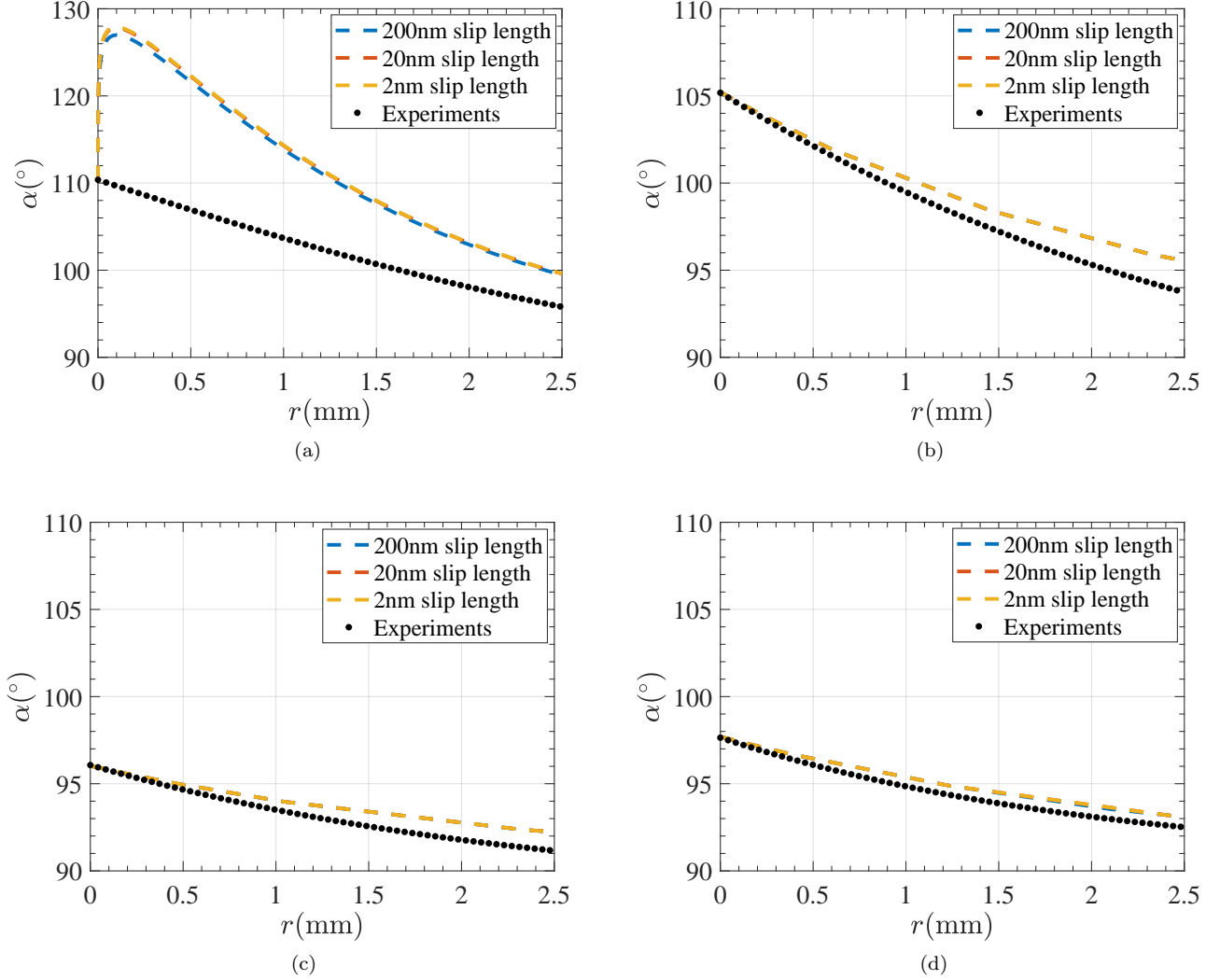


FIG. 13: Same as figure 8 with only difference in contact angle employed at the contact line. Dynamic contact angle (θ_d) is used instead of θ_e . (a) air-500 cSt silicone oil at $Ca = 8.37 \times 10^{-2}$, $\theta_d = 110.4$; $c = 0.54$; (b) air-sugar 60% at $Ca = 1.04 \times 10^{-4}$, $\theta_d = 105.2$; $c = 0.68$ over a hydrophobic coated solid surface. (c) air-sugar 48% at $Ca = 8.16 \times 10^{-5}$, $\theta_d = 96$; $c = 0.94$ over a hydrophobic coated solid surface. (d) air-water at $Ca = 1.24 \times 10^{-5}$, $\theta_d = 97.7$; $c = 0.88$ over a hydrophobic coated solid surface.

This is illustrated schematically in figure 14(a) and algorithmically written as

$$\psi_{(i+1,j)} = \psi_{(i,j)} + \frac{v_{(i,j)} + v_{(i+1,j)}}{2} \Delta x \quad (\text{E1})$$

where Δ_x is the horizontal distance between (i,j) and $(i+1,j)$. Having determine $\psi_{(i+1,j)}$, we can then determine $\psi_{(i+1,j+1)}$ as

$$\psi_{(i+1,j+1)} = \psi_{(i+1,j)} + \frac{u_{(i+1,j)} + u_{(i+1,j+1)}}{2} \Delta y. \quad (\text{E2})$$

This process is sequentially followed over the entire domain. Since the vertical wall, represented by $i = 1$, represents a streamline, the streamfunction value is constant along the wall. We set $\psi_{1,j} \equiv 0$ consistent with the boundary condition for streamfunction in theoretical models. Note that the first grid point, i.e. $i = 1$, is not at the wall, but at the offset location shown in figure 14(b). The maximum error this causes is about 8 pixels, roughly about $32 \mu\text{m}$. This means that theoretical and experimental streamfunction contours could be displaced from each other horizontally by a maximum of $32 \mu\text{m}$. At the scale of the flow field which is approximately $\tilde{O}(mm)$ or $\tilde{O}(1000 \mu\text{m})$, this error is deemed to be within acceptable limits.

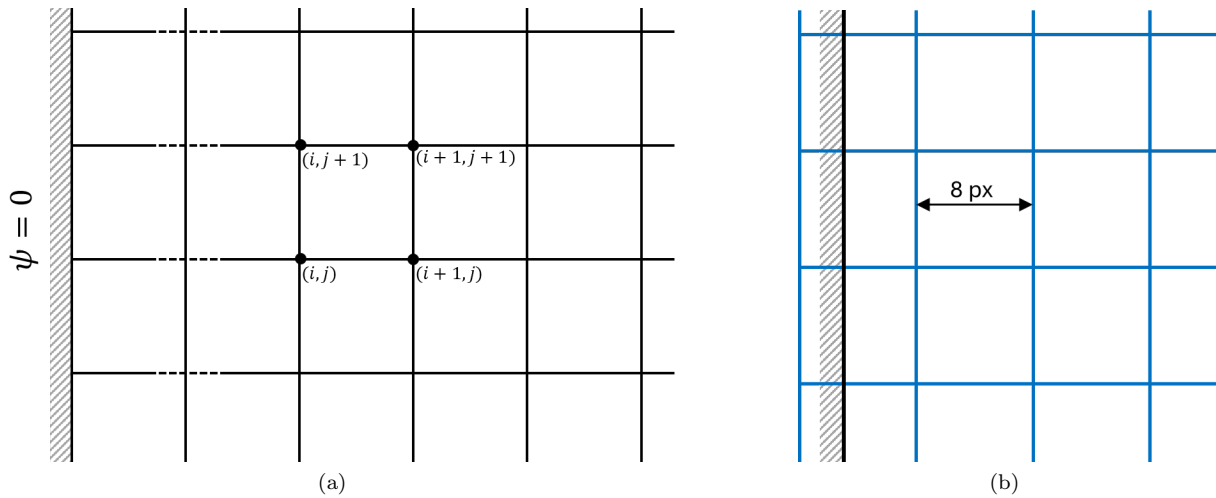


FIG. 14: (a) Schematic representation of the PIV grid to calculate streamfunction, (b) A schematic view of the interrogation window coincident with the physical space containing the moving plate. The typical interrogation window size used in the experiments is $16 \text{ px} \times 16 \text{ px}$ with an offset of $8 \text{ px} \times 8 \text{ px}$. This provides the upper bound for the location of the first grid point where a velocity vector is obtained.

-
- [1] C. Huh and L. E. Scriven, Hydrodynamic model of steady movement of a solid/liquid/fluid contact line, *J. Colloid Interface Sci.* **35**, 85 (1971).
 - [2] T. Blake and J. Haynes, Kinetics of liquid/liquid displacement, *J. Colloid Interface Sci.* **30**, 421 (1969).
 - [3] P.-G. De Gennes, Wetting: statics and dynamics, *Rev. Mod. Phys.* **57**, 827 (1985).
 - [4] O. Voinov, Hydrodynamics of wetting, *Fluid Dyn.* **11**, 714 (1976).
 - [5] R. Cox, The dynamics of the spreading of liquids on a solid surface. part 1. viscous flow, *J. Fluid Mech.* **168**, 169 (1986).
 - [6] Y. D. Shikhmurzaev, The moving contact line on a smooth solid surface, *Int. J. Multiph. Flow* **19**, 589 (1993).
 - [7] E. Dussan, On the spreading of liquids on solid surfaces: static and dynamic contact lines, *Annual Review of Fluid Mechanics* **11**, 371 (1979).
 - [8] J. H. Snoeijer and B. Andreotti, Moving contact lines: scales, regimes, and dynamical transitions, *Annual review of fluid mechanics* **45**, 269 (2013).
 - [9] Y. D. Shikhmurzaev, *Capillary flows with forming interfaces* (Chapman and Hall/CRC, 2007).
 - [10] Y. D. Shikhmurzaev, Moving contact lines in liquid/liquid/solid systems, *J. Fluid Mech.* **334**, 211 (1997).
 - [11] E. Kirkinis and S. H. Davis, Hydrodynamic theory of liquid slippage on a solid substrate near a moving contact line, *Physical Review Letters* **110**, 234503 (2013).
 - [12] E. Kirkinis and S. Davis, Moffatt vortices induced by the motion of a contact line, *J. Fluid Mech.* **746** (2014).
 - [13] M. Febres and D. Legendre, Existence of moffatt vortices at a moving contact line between two fluids, *Phys. Rev. Fluid* **2**, 114002 (2017).
 - [14] H. K. Moffatt, Viscous and resistive eddies near a sharp corner, *Journal of Fluid Mechanics* **18**, 1 (1964).
 - [15] E. Ramé, S. Garoff, *et al.*, On identifying the appropriate boundary conditions at a moving contact line: an experimental investigation, *J. Fluid Mech.* **230**, 97 (1991).
 - [16] T. S. Chan, S. Srivastava, A. Marchand, B. Andreotti, L. Biferale, F. Toschi, and J. H. Snoeijer, Hydrodynamics of air entrainment by moving contact lines, *Physics of fluids* **25** (2013).
 - [17] T. S. Chan, C. Kamal, J. H. Snoeijer, J. E. Sprittles, and J. Eggers, Cox–voinov theory with slip, *Journal of fluid mechanics* **900**, A8 (2020).
 - [18] Y. Kulkarni, T. Fullana, and S. Zaleski, Stream function solutions for some contact line boundary conditions: Navier slip, super slip and the generalized navier boundary condition, *Proc. R. Soc. A* **479**, 20230141 (2023).
 - [19] E. DUSSAN V and S. DAVIS, On the motion of a liquid interface along a solid surface, *J. Fluid Mech.* **65**, 7195 (1974).
 - [20] R. L. Hoffman, A study of the advancing interface. i. interface shape in liquid–gas systems, *Journal of colloid and interface science* **50**, 228 (1975).
 - [21] Q. Chen, E. Ramé, and S. Garoff, The breakdown of asymptotic hydrodynamic models of liquid spreading at increasing capillary number, *Phys. Fluids* **7**, 2631 (1995).
 - [22] E. Ramé and S. Garoff, Microscopic and macroscopic dynamic interface shapes and the interpretation of dynamic contact angles, *J. Colloid Interface Sci.* **177**, 234 (1996).
 - [23] Q. Chen, E. Ramé, and S. Garoff, The velocity field near moving contact lines, *J. Fluid Mech.* **337**, 49 (1997).
 - [24] N. Le Grand, A. Daerr, and L. Limat, Shape and motion of drops sliding down an inclined plane, *Journal of Fluid Mechanics* **541**, 293 (2005).

- [25] E. Rio, A. Daerr, B. Andreotti, and L. Limat, Boundary conditions in the vicinity of a dynamic contact line: experimental investigation of viscous drops sliding down an inclined plane, *Physical review letters* **94**, 024503 (2005).
- [26] B. A. Puthenveetil, V. K. Senthilkumar, and E. Hopfinger, Motion of drops on inclined surfaces in the inertial regime, *J. Fluid Mech.* **726**, 26 (2013).
- [27] C. Gupta, A. Sangadi, L. D. Chandrala, and H. N. Dixit, A study of flow patterns near moving contact lines over hydrophobic surfaces, in *Conference on Fluid Mechanics and Fluid Power* (Springer, 2022) pp. 339–349.
- [28] C. Gupta, A. Choudhury, L. D. Chandrala, and H. N. Dixit, An experimental study of flow near an advancing contact line: a rigorous test of theoretical models, *Journal of fluid mechanics* **1000**, A45 (2024).
- [29] C. Gupta, L. D. Chandrala, and H. N. Dixit, An experimental investigation of flow fields near a liquid–liquid moving contact line, *The European Physical Journal Special Topics* , 1 (2024).
- [30] C. Duez, C. Ybert, C. Clanet, and L. Bocquet, Making a splash with water repellency, *Nature physics* **3**, 180 (2007).
- [31] D. N. Sibley, A. Nold, and S. Kalliadasis, The asymptotics of the moving contact line: cracking an old nut, *J. Fluid Mech.* **764**, 445 (2015).
- [32] J. H. Snoeijer, Free-surface flows with large slopes: Beyond lubrication theory, *Physics of Fluids* **18** (2006).